Phase-locked stereoscopic PIV measurements of the turbulent swirling flow in a dynamic model of a uniflow-scavenged two-stroke engine cylinder

Ingvorsen, Kristian Mark; Meyer, Knud Erik; Walther, Jens Honore; Mayer, Stefan

Published in:
Proceedings of the 10th International Symposium on Particle Image Velocimetry

Publication date:
2013

10TH INTERNATIONAL SYMPOSIUM ON PARTICLE IMAGE VELOCIMETRY - PIV13
Delft, The Netherlands, July 1-3, 2013

Phase-locked stereoscopic PIV measurements of the turbulent swirling flow in a dynamic model of a uniflow-scavenged two-stroke engine cylinder

Kristian Mark Ingvorsen[1], Knud Erik Meyer[1], Jens Honoré Walther[1,2], and Stefan Mayer[3]

[1] Department of Mechanical Engineering, Technical University of Denmark, Kgs. Lyngby, Denmark
kmin@mek.dtu.dk

[2] Computational Science and Engineering Laboratory, ETH Zürich, Zürich, Switzerland

[3] MAN Diesel & Turbo SE, Copenhagen, Denmark

ABSTRACT

It is desirable to use computational fluid dynamics for the optimization of in-cylinder processes in large two-stroke low-speed uniflow-scavenged marine diesel engines. However, the complex nature of the turbulent swirling in-cylinder flow necessitates experimental data for validation of the used turbulence models. In the present work, the flow in a dynamic scale model of a uniflow-scavenged cylinder is investigated experimentally. The model has a transparent cylinder and a movable piston driven by a linear motor. The flow is investigated using phase-locked stereoscopic particle image velocimetry (PIV) and time resolved laser Doppler anemometry (LDA). Radial profiles of the phase-averaged mean velocities are computed from the velocity fields recorded with PIV and the validity of the obtained profiles is demonstrated by comparison with reference LDA measurements. Radial profiles are measured at five axial positions for 15 different times during the engine cycle and shows the temporal and spatial development of the swirling in-cylinder flow. The tangential velocity profiles in the bottom of the cylinder near the end of the scavenging process are characterized by a concentrated swirl resulting in wake-like axial velocity profiles and the occurrence of a vortex breakdown. After scavenge port closing the axial velocity profiles indicate that large transient swirl-induced structures exists in the cylinder. Comparison with profiles obtained under steady-flow conditions shows that the steady profiles in general will not be representative for the dynamic conditions. The temporal development of the swirl strength is investigated by computing the angular momentum. The swirl strength shows an exponential decay from scavenge port closing to scavenge port opening corresponding to a reduction of 34%.

1. Introduction

1.1 Background and motivation

Large two-stroke low-speed uniflow-scavenged marine diesel engines are used to power the largest marine vessels such as tankers and container ships. A key process for these engines is the scavenging process [15]. The scavenging process is the gas exchange where the combustion gas from the previous cycle is replaced by fresh air for the next cycle. Large two-stroke low-speed marine diesel engines use the uniflow scavenging method in a configuration with scavenge ports located in the cylinder liner near the bottom of the cylinder and a single centered exhaust valve in the cylinder head. As the piston approaches the bottom dead center (BDC), it uncovers the scavenge ports and compressed air is blown into the cylinder forcing the combustion gas out through the exhaust valve in a combined displacement and mixing process. The scavenge ports are cut at an angle, typically in the range 15-25°, with respect to the radial direction creating a swirling in-cylinder flow. The swirl improves the scavenging process and enhances the fuel-air mixing during the combustion phase [5]. In addition, the scavenging flow also provides cooling of the combustion chamber surfaces. To reduce emission levels, enhance engine efficiency, and analyze combustion chamber temperatures it is desirable to use computational fluid dynamics (CFD) simulations. However, turbulent swirling flows, such as the in-cylinder flow in a uniflow-scavenged engine, are known to be very difficult to predict using CFD tools owing to their complex nature [9]. Experimental results are therefore needed in order to serve as validation data and to aid the development of turbulence models. Despite the need for experimental data on the turbulent swirling flow in uniflow-scavenged engines almost no works exist in the open literature presenting results suitable for validation purposes. It is this lack of experimental data that has motivated the present work.

1.2 Previous work

The swirling in-cylinder flow in uniflow-scavenged engines have been the subject of earlier works, and investigations have been based on both CFD (e.g. [19, 2, 20, 3, 13, 17]) and experiments (e.g. [14, 12, 16, 4, 8, 7]). Due to the costs and limitations of experimental investigations on full-scale engines the majority of the experimental work have been performed on simplified scale models, and often under steady-flow conditions. Ingvorsen et al. [7] developed a simplified experimental scale model of the MAN Diesel & Turbo 4T50ME-X research engine [6], which is a production sized low-speed marine diesel engine. The flow in the model was investigated under steady-flow conditions through extensive measurements using stereoscopic particle image velocimetry (PIV) and laser Doppler anemometry (LDA). For a 20° port angle, it was found, that the radial profiles of tangential velocity correspond to a concentrated vortex, with the highest velocities occurring near the cylinder axis. The axial profiles have a wake-like shape created by a velocity deficit at the axis. In the bottom of the cylinder a central recirculation zone exists and near the cylinder head the vortex core is observed

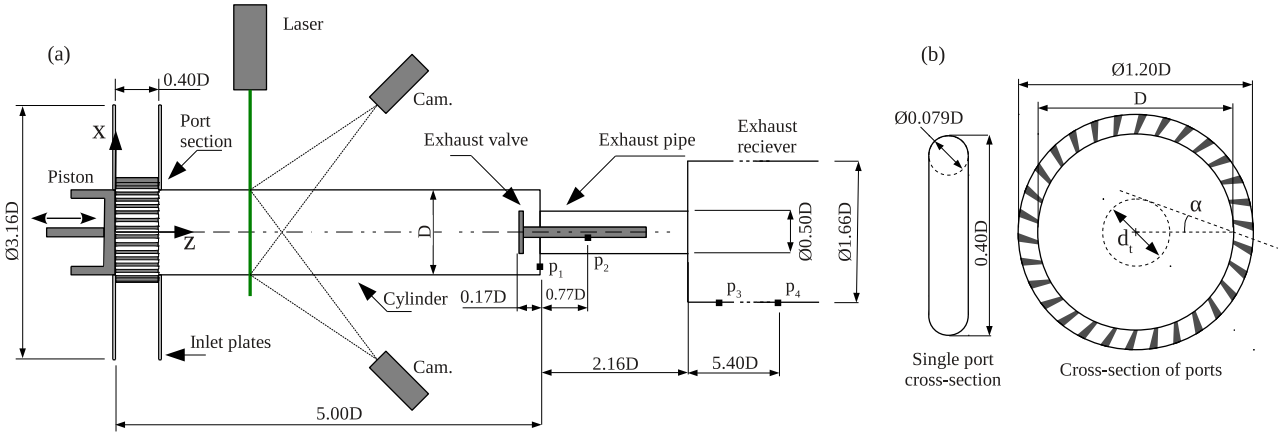

Figure 1: (a) Sketch of the model and optical setup. (b) Details of the port section geometry. Adapted from [7].

to precess around the exhaust valve.

1.3 Present work

The present work extends the work by Ingvorsen et al. [7] by considering the flow in the engine model under dynamic conditions, where the ports are opened and closed by the piston. The main purpose of the reported work is to establish a database of validated data that can be used in the development and validation of CFD models. Secondly, the work should increase the understanding of the in-cylinder flow field under dynamic conditions and make it possible to evaluate to which degree the results found under steady-flow conditions represent the flow under dynamic conditions.

For the investigations a simplified scale model with a moving piston and a transparent cylinder is used [7]. The design of the model ensures that the dynamics of the in-cylinder swirling flow are similar to the dynamics of the flow in the full-scale engine. Due to practical limitations compression and combustion are neglected in the model. The experiments are thus carried out under iso-thermal conditions, with both the combustion gas and scavenge air represented by ambient air at room temperature. The turbulent swirling flow in the cylinder is measured using phase-locked stereoscopic PIV and LDA.

2. Methodology

2.1 Problem scaling

To ensure that the flow dynamics in the experimental scale model are similar to the dynamics in a full scale engine, a short analysis is carried out considering the main parameters characterizing the scavenge flow in a uniflow-scavenged engine. For the analysis the characteristic scavenge velocity is introduced as $U_{sc} = m_{sc}(\rho t_{sc} A_{cyl})^{-1}$, where m_{sc} is the mass of scavenged gas per cycle, ρ is the gas density, A_{cyl} is the cross-sectional area of the cylinder, and t_{sc} is the scavenge time. In the present work the scavenge time refers to the time from scavenge port opening t_{SPO} to scavenge port closing t_{SPC} such that $t_{sc} = t_{SPC} - t_{SPO}$. Using the scavenge velocity, the flow dynamics can be characterized by the following three non-dimensional quantities; (i) the Reynolds number $Re = U_{sc}D/\nu$, where D is the cylinder diameter and ν is the kinematic viscosity of the gas, (ii) the non-dimensional scavenge velocity $U^*_{sc} = U_{sc}t_{sc}/D$, and (iii) the non-dimensional scavenge time $t^*_{sc} = t_{sc}/t_{cyc}$, where t_{cyc} is the period of the engine cycle. It should be noted that the non-dimensional scavenge velocity U^*_{sc} is directly related to the delivery ratio as well as the engine Strouhal number. The engine Strouhal number $Sr = nD/U_{sc}$, where n is the engine speed, has been shown to be an important similarity parameter when modeling the scavenging process [1]. To ensure similarity of the flow dynamics, the three non-dimensional parameters should ideally be identical for the experimental model and the full scale engine.

In the 4T50ME-X research engine the non-dimensional parameters are $Re = 2{,}600{,}000$, $U^*_{sc} = 5.2$, and $t^*_{sc} = 0.21$ [17]. The non-dimensional scavenge velocity and time can be matched, however due to the practical limitations it is not possible to reach such high Reynolds numbers in the experimental model. It is, however, known that the mean flow becomes approximately independent of the Reynolds number for sufficiently large Reynolds numbers. In the steady-flow investigations it was shown that both the mean and rms-velocities becomes independent of the Reynolds number for $Re \gtrsim 50{,}000$ [7]. The required scavenge velocity and scavenge time for the experimental model, can therefore be determined from the model diameter D and requiring that the model Reynolds number is $Re \gtrsim 50{,}000$.

2.2 Flow rig

A schematic of the experimental model is presented in Figure 1 and a detailed description of the experimental setup is given in [7]. In short, the model consist of a transparent glass cylinder with an internal diameter of $D = 190\,\text{mm}$. The flow enters the cylinder through a port section placed in the bottom of the glass cylinder. The total length of the cylinder measured from the bottom of the ports to the cylinder head is $5.00D$. The port section can be changed making it possible to test different port configurations with, for example, different port angles and shapes and different number of ports. The port configuration used for the present investigations is shown in Figure 1b and has 30 equally spaced ports with a port angle of $\alpha = 20^\circ$ and a port height of $0.40D$. Two inlet plates are used to guide

the ambient air from the surroundings to the ports. The flow exits the cylinder through an exhaust pipe with a diameter of $0.50D$. To enter the exhaust pipe the flow must go around a static exhaust valve with an opening corresponding to full valve lift in the engine. From the exhaust pipe the flow enters the exhaust receiver which is a large cylindrical volume with a diameter of $1.66D$ and length of $6.77D$. The exhaust receiver is connected to a frequency controlled centrifugal fan by a contraction. The fan drives the flow through the model and exhausts directly into the ambient air. Both the cylinder head, the exhaust valve, and the piston surface are flat. The gap between the piston side and cylinder wall is $0.005D$ and is sealed by two custom made piston rings. The piston rings are made in Teflon to reduce friction and limit abrasion of the glass wall. The axial distance from the piston surface to the contact point between the first piston ring and the cylinder wall is $0.03D$, meaning that the effective port opening occurs slightly before the piston surface moves below the top of the scavenge ports. A coordinate system is defined as shown in Figure 1a with the z-axis coincident with the cylinder axis and the origin at the axial position corresponding to the bottom of the ports.

The piston motion is controlled by a linear motor and a programmable servo controller. At the cycle start the piston is located with the piston surface at $z/D = 1.00$, it then moves to $z/D = 0.00$, corresponding to 100% open ports, and back to $z/D = 1.00$ in a sinusoidal motion. Having returned to $z/D = 1.00$ the piston has a standstill period before the cycle is repeated. The total cycle time is $t_{cyc} = 1.20\,\mathrm{s}$ and both the motion and standstill period are $\frac{1}{2}t_{cyc}$ in duration. Defining the time of port opening and closing as the times when the piston surface is at $z/D = 0.40D$, the port opening and closing occur at $t_{SPO} = 0.14t_{cyc}$ and $t_{SPC} = 0.36t_{cyc}$, respectively. To relate the velocity and pressure measurements to the piston motion a trigger signal is sent from the servo controller at port opening. The fan speed is adjusted such that the Reynolds number based on the scavenge velocity is $Re = 50{,}000$, which for standard ambient conditions (20° C, 1 atm) corresponds to $U_{sc} = 3.96\,\mathrm{m/s}$. The non-dimensional scavenge velocity and scavenge time for the model thus become $U^*_{sc} = 5.4$ and $t^*_{sc} = 0.22$, respectively. These are approximately the same as in the full-scale engine and it can therefore be expected that the flow physics in the model and the engine are similar. It should be noted, that when adjusting the fan speed, the scavenge velocity is estimated from time resolved measurements of the pressure difference over the valve using a pressure drop coefficient determined under steady-flow conditions.

The scavenge velocity based on the pressure difference is not sufficiently accurate for normalization purposes. Instead, the bulk velocity at $t/t_{cyc} = 0.25$, corresponding to fully open ports, is used to normalize the results in the remainder of the paper. The bulk velocity is denoted V_b and is estimated from the radial profile of axial velocity measured with PIV at $z/D = 1.50$, and is found to be $V_b = 4.70\,\mathrm{m/s}$. The PIV and LDA measurements are performed at five axial positions corresponding $z/D = \{1.00, 1.50, 2.00, 3.00, 4.00\}$

2.3 Pressure measurements

The pressure in the model is measured using four wall pressure tabs. The pressure tabs are located in the cylinder head, on the exhaust valve rod, and on the side of the exhaust receiver $0.37D$ and $5.40D$ downstream the inlet to the exhaust receiver c.f. Figure 1a. The pressure is measured with pressure transducers and sampled with a rate of 5.0 kHz using a LabVIEW acquisition system. The pressure is measured for 50 consecutive cycles and the phase-averaged pressure is calculated.

2.4 Laser Doppler anemometry (LDA)

The details of the used laser Doppler anemometry (LDA) system are given in [7]. Due to the optical distortions created by the curved glass wall, the LDA system is limited to measurements of the axial velocity component in a horizontal plane going through the cylinder axis. The system is operated in burst mode which results in velocity measurements randomly distributed in time. In order to estimate the phase-averaged velocity, a temporal binning is carried out using a window size of $10^{-3}t_{cyc}$. The seeding used for the measurements is di-ethyl-hexyl-sebacate (DEHS) droplets with diameters in the range 0.1–2.0 μm generate by a Laskin nozzle.

2.5 Stereoscopic particle image velocimetry (PIV)

System:

Stereoscopic particle image velocimetry (PIV) measurements are carried out using a commercial PIV system consisting of two cameras and a laser. The laser is a 200 mJ double cavity Nd:YAG laser. The light sheet thickness in the field of view is 2–3 mm and the laser is operated at full power for the measurements. The cameras are 12 bit gray-scale CCD cameras (Dantec Dynamics HiSense Mk II) with a chip size of $1{,}344 \times 1{,}024$ pixels and a pixel pitch of 6.45 μm. The cameras are fitted with 60 mm lenses using Scheimpflug mounts and the F-number is set to 11 for both cameras. A schematic of the PIV setup is included in Figure 1. The laser is positioned next to the model such that the light sheet illuminates the cylinder cross section. The cameras are positioned at the downstream side of the light sheet with one camera on the same side as the laser (backward scatter position) and one camera on the opposite side of the cylinder (forward scatter position). Due to the angular dependency of the intensity for Mie scattering, the camera in the backward scatter position receives significantly less light than the camera in the forward scatter position. This difference is accounted for by increasing the gain level on the camera in the backward scatter position. The laser and cameras are mounted on a traverse aligned with the cylinder axis allowing measurements to be taken at different axial positions using the same camera calibration. The camera calibration, acquisition, and processing of particle images are carried out using the Dantec Dynamics DynamicStudio version 3.3 software. Before analyzing the particle images, background images are subtracted to enhance the image quality. The used background images are calculated as the temporal minimum image of their respective measurement series. The particle images are processed using a three-step adaptive correlation algorithm with a final interrogation area size of 32×32 pixels and 50% overlap. Spurious vectors are detected using a local median criterion and replaced by interpolation.

To obtain phase-locked measurements, the timing of the laser and cameras is controlled by the trigger signal sent from the servo-controller. By specifying a trigger delay in the software, it is possible to measure at arbitrary times during the cycle. Measurements are performed at 15 different times during the cycle. The measurement times are presented in Table 1 together with the corresponding piston positions, and port opening ratios.

Table 1: Measurement times for the PIV measurements together with the corresponding piston position and port opening ratios.

t/t_{cyc}	z/D	Port opening	t/t_{cyc}	z/D	Port opening
0.00	1.00	-	0.34	0.30	25% open
0.10	0.65	-	0.40	0.65	-
0.16	0.30	25% open	0.50	1.00	-
0.18	0.20	50% open	0.60	1.00	-
0.20	0.10	75% open	0.70	1.00	-
0.25	0.00	100% open	0.80	1.00	-
0.30	0.10	75% open	0.90	1.00	-
0.32	0.20	50% open			

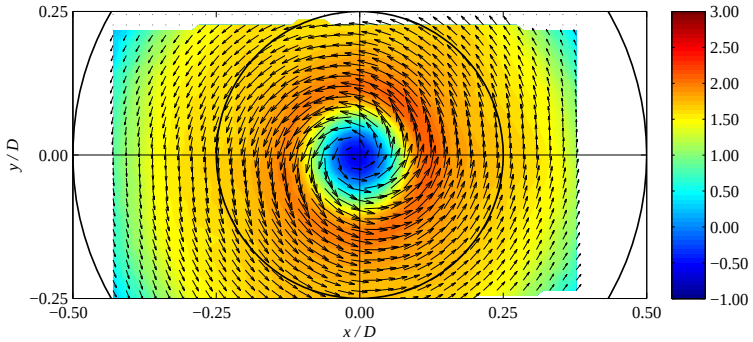

Figure 2: Phase-averaged mean velocity field at $z/D = 1.00$ and $t/t_{cyc} = 0.30$. The in-plane velocities V_r and V_θ are shown by vectors and the axial velocities V_z/V_b are shown by color. Every second vector in each direction is shown.

Post processing:
For each measurement point, corresponding to a given time and axial position, the three-component instantaneous velocity field v_i, $i = 1,2,3$ is recorded for 100 consecutive cycles. The ensemble average and standard deviation, corresponding to the phase-averaged mean velocity field V_i and the phase-averaged rms-field $V_{i,\mathrm{rms}}$, are calculated for each measurements series based on the 100 samples. An example of the phase-averaged velocity field is shown in Figure 2. The field of view covers an approximately rectangular region with the left corners close to the cylinder wall. The phase-averaged mean and rms-velocity fields are observed to be approximately axisymmetric. It is therefore convenient to represent them using a cylindrical coordinate system with coordinates r, θ, z and corresponding velocity components V_r, V_θ, V_z. The mean and rms-velocity fields are converted to radial profiles by averaging in the θ-direction which in practice is done by performing a radial binning (see [7] for details).

Due to the inevitable inaccuracies of the experimental setup, the swirl center of the phase-averaged mean field will in general not coincide exactly with the cylinder center. This phenomenon is most pronounced for measurements taken shortly after the port opening, where the flow is subjected to large changes without having been stabilized by a strong swirl as later in the cycle. To account for the difference between the swirl center and geometrical center, the radial profiles in the range $r/D = 0.00$–0.30 are generated using the swirl center as the coordinate system origin, while the profiles in the range $r/D = 0.30$–0.50 are generated using the geometrical center as origin.

Profile accuracy:
The accuracy of the radial velocity profiles obtained from the PIV measurements are evaluated both by comparing profiles from repeated measurement series as well as comparing the PIV profiles with reference profiles measured with LDA.

Repeated measurements are carried out at the axial position $z/D = 1.00$ for $t/t_{cyc} = 0.25$ and $t/t_{cyc} = 0.30$. The comparison of the profiles is presented in Figure 3 and shows a high repeatability. The mean discrepancy between the profiles is found to be 3% of V_b. It is noted that the largest uncertainties are observed for the axial velocity component near the center and close to the wall. One reason for this, is that the statistical basis near the center and wall is smaller than at the mid-radius region, due to the radial binning. It is further noted, that the agreement of the profiles at $t/t_{cyc} = 0.30$ is higher than at $t/t_{cyc} = 0.25$, and indicates that the increase in swirl strength has stabilized the flow making the measurements more repeatable.

The axial velocity profiles obtained by PIV can be compared to the LDA measurements. In this case a comparison can be made for all axial positions and for all cycle times. Examples of the comparison are shown in Figure 4 for the times $t/t_{cyc} = 0.25$ and $t/t_{cyc} = 0.30$. The comparison shows a good agreement between the PIV and LDA profiles with a mean discrepancy of 6% of V_b. It should however be noted, that the profiles are not directly comparable, as they are generated in different ways. The main difference is that the LDA profiles are measured at the horizontal plane going through the cylinder center. This means that the LDA profiles in general will not go exactly through the mean swirl center which is ensured for the PIV profiles due to the post-processing. Discrepancies between the profiles are therefore not entirely due to uncertainties in the measurements, but also the consequence of comparing two different types of profiles.

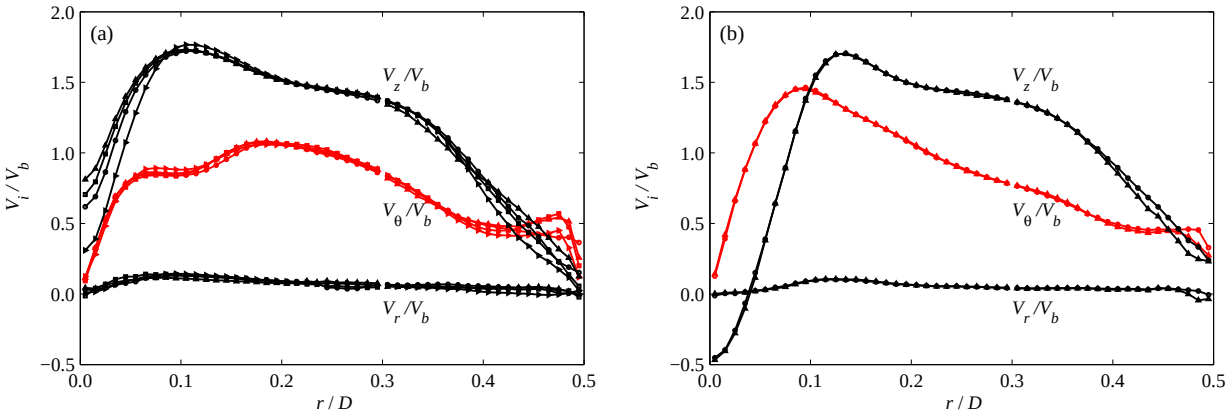

Figure 3: Comparison of repeated PIV measurements at $z/D = 1.00$ for two different times. (a) $t/t_{cyc} = 0.25$, (b) $t/t_{cyc} = 0.30$

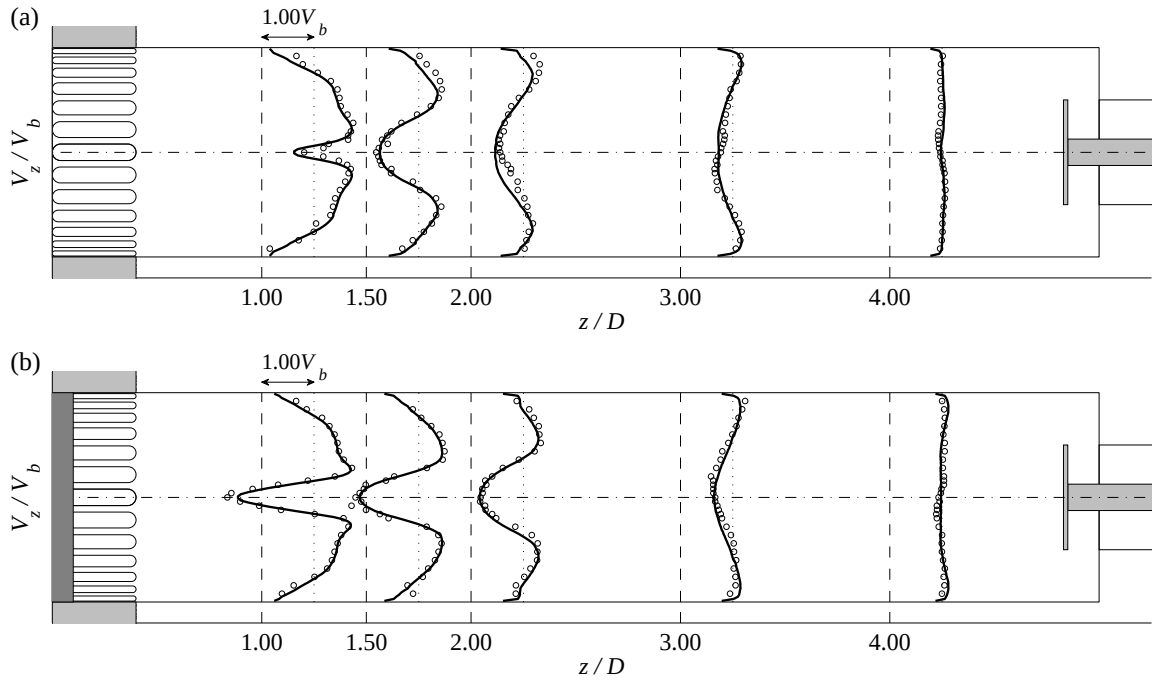

Figure 4: Example of comparison of radial profiles of axial velocity measured with PIV (*solid lines*) and LDA (*open circles*). (a) $t/t_{cyc} = 0.25$, (b) $t/t_{cyc} = 0.30$.

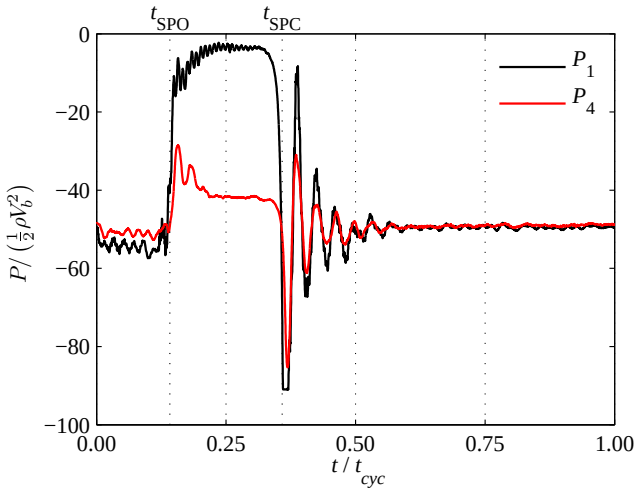

Figure 5: Phase-averaged pressure P as a function of time measured at the cylinder head P_1 and at the exhaust receiver outlet P_4.

3. Results

3.1 Pressure

The phase-averaged pressure at the cylinder head P_1 and at the exhaust receiver outlet P_4 are presented in Figure 5. At scavenge port opening a rapid increase is observed at both locations. The pressure at the cylinder head continues to increase reaching an approximately constant value at $t/t_{cyc} = 0.23$. During the scavenging fast oscillations are observed in the cylinder pressure with a frequency of $f = c/(4L)$, where c is the speed of sound and L is the cylinder length. This is the fundamental frequency for a cylinder with one end open and one end closed [21]. This shows that the bottom end of the cylinder acts as an open end when the ports are uncovered while the top end acts as closed even though the exhaust valve is open. This behavior is consistent with oscillations observed in measurements and simulations of a full-scale fired engine [17].

After the initial increase following the port opening the pressure at the exhaust receiver outlet P_4 is reduced again, reaching an approximately constant value of $P/\left(\frac{1}{2}\rho V_b^2\right) = 42$ at $t/t_{cyc} = 0.23$. At scavenge port closing (SPC) both pressures show a rapid reduction resulting in a new series of large oscillations. The oscillations after port closure are significantly slower than the in-cylinder oscillations observed under scavenging and are expected to be the result of a Helmholtz resonator phenomenon where the cylinder and exhaust receiver volumes acts as springs and the exhaust pipe volume acts as a mass. The oscillations are quickly damped out and the pressure becomes approximately constant at $t/t_{cyc} = 0.60$.

3.2 Flow rate

The phase-averaged flow rate Q' through the cylinder during the period with piston motion ($t/t_{cyc} = 0.00$–0.50) is shown in Figure 6. The flow rate is estimated by integrating the radial profiles of axial velocity obtained from the PIV and LDA measurements at $z/D = 1.50$. The flow rate estimated from the pressure difference over the exhaust valve is also included. It is expected that the flow rate estimated from the PIV profiles is the most accurate, however the estimates based on the LDA and pressure measurements are time resolved and therefore give a more complete description of the flow development. In general good agreement is observed between the PIV and LDA estimates, while the estimates based on the pressure difference over the exhaust valve shows a lag after port opening and a lower maximum flow rate. The larger uncertainties on the estimates based on the pressure difference compared to the PIV and LDA estimates are expected, as the used pressure drop coefficient was obtained under steady-flow conditions.

From the cycle start to the scavenge port opening, the flow rate is negative due to the downward motion of the piston c.f. Figure 6. After port opening the flow direction changes and the flow rate increases to an approximately constant value shortly before the piston reaches $z/D = 0.00$. The flow rate remains approximately constant until the ports are almost completely covered, at which point it shows a rapid decrease. The relatively slow change in flow rate at port opening compared to port closing, is the result of fluid inertia. At the time of port opening the air is being pulled into the cylinder through the exhaust valve by the piston motion. The flow direction therefore has to change before the scavenging can commence. This is different to the process in a fired engine, where the gas is being blown out of the cylinder before port opening due to the high in-cylinder pressure created by the combustion.

3.3 Phase-averaged velocity profiles

The radial profiles of phase-averaged tangential V_θ and axial velocity V_z are presented in Figure 7 and 8 for different times during the cycle. To aid the interpretation of the results, the profiles are plotted in the model geometry, where also the piston position is shown. The axial profiles are mirrored in the cylinder axis and the tangential profiles are mirrored both in the cylinder axis and the datum lines.

Considering first the development of the tangential velocity (Figure 7–8, *top row*) the following is noted. At the cycle start $t/t_{cyc} = 0.00$ a pre-swirl or residual swirl exist and the swirl strength is approximately the same for the different axial positions. The profiles consist of a central region where the velocity increases with radial position, an annular region where the velocity is approximately constant or slightly decreasing as a function of radial position, and a thin wall boundary layer where the velocity shows a rapid decrease. For

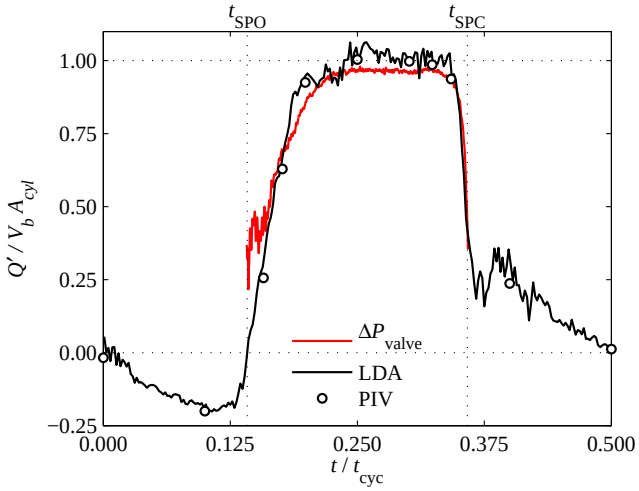

Figure 6: Phase-averaged flow rate during piston motion estimated from the PIV and LDA profiles and the pressure difference over the exhaust valve (ΔP_{valve}).

$t/t_{cyc} = 0.10$ and $t/t_{cyc} = 0.16$ the profiles show no or limited effect of the downward motion of the piston and the port opening. At $t/t_{cyc} = 0.18$ an increase in the tangential velocity near the wall is observed for the $z/D = 1.00$ profile showing that the scavenge air has now penetrated to this axial position. At $t/t_{cyc} = 0.20$ the tangential velocity at $z/D = 1.00$ is significantly increased and the position of the maximum velocity has moved closer to the wall and is approximately at $r/D = 0.30$. The introduction of swirl can now also be observed at the $z/D = 1.50$ profile. At $t/t_{cyc} = 0.25$, corresponding to fully open ports, the maximum tangential velocity is further increased and the profile shape becomes complex with two local maximum positions. The profiles at $z/D = 1.50$ and $z/D = 2.0$ are also significantly affected showing approximately solid body rotation in the central region with maximum velocities at approximately $r/D = 0.30$. At $t/t_{cyc} = 0.30$, corresponding to 25% closed ports, the tangential profile at $z/D = 1.00$ has the maximum velocity close to the center axis with the highest observed tangential velocity for the entire cycle. The profile shape corresponds to a concentrated vortex [18] and is similar to the profiles found in the steady-flow case [7]. The radial profile now consists of a small central region with a high gradient and an approximately solid body rotation, and an annular region where the velocity decreases as a function of the radial position. The tangential profiles near the cylinder head, have not obtained this profile shape and still have the maximum velocity close to the wall. At $t/t_{cyc} = 0.32$ the ports are 50% closed and the maximum swirl velocity is reduced at the first two axial positions while it is slightly increased at the downstream positions. The swirl profiles show non-monotonic behavior near the cylinder wall. At $t/t_{cyc} = 0.34$ the ports are 75% closed and the tangential profile at $z/D = 1.00$ have become highly complex with multiple local maximum values. The profiles for $z/D = 1.50$ and $z/D = 2.00$ are less affected and shows a small reduction in maximum swirl velocity while the profiles for $z/D = 3.00$ and 4.00 show a small increase. The swirl velocity for the $z/D = 4.00$ position is approximately constant except very close to the center and the wall. At $t/t_{cyc} = 0.40$ the scavenge ports have closed and a large change in velocity profiles are observed for the first three positions. They become similar to the downstream profiles where the central region has an approximately solid body rotation and the annular region has approximately constant velocity. At $t/t_{cyc} = 0.50$ the piston has returned to $z/D = 1.00$, the profiles at $z/D = 1.50$ and 2.00 show approximately solid body rotation over the majority of the cross section with only a thin boundary layer on the wall. In the remaining standstill period ($t/t_{cyc} = 0.60$–1.00), the profiles in general become more similar for the different axial positions, showing a rapid increase from the center followed by an annular region with approximately constant velocity.

Inspecting the radial profiles of axial velocity (Figure 7–8, *bottom row*) it is seen that at the cycle start $t/t_{cyc} = 0.00$ negative axial velocities exist near the cylinder axis for all axial positions. It is expected that the non-zero axial velocities are caused by the residual swirl. At $t/t_{cyc} = 0.10$ negative velocities are observed over the entire cross section for all axial positions showing that the air is pulled down by the piston. At $t/t_{cyc} = 0.16$ the flow direction has changed and positive axial velocities are observed for all axial positions. The profile at $z/D = 1.00$ has a small peak near the wall showing that air is blown into the cylinder in an annular region close to the liner. The profiles for $z/D = 1.50$ and 2.00 are approximately constant while the two last profiles show a peak near the cylinder axis. The peak is expected to be caused by a suction effect along the swirl center and a similar effect was observed for the steady-flow case [7].

At $t/t_{cyc} = 0.18$ the general trend is unchanged but the magnitude of the velocities has increased. The shape of the first axial profile is wake-like with a wide deficit. At $t/t_{cyc} = 0.20$ the wake-like shape becomes more pronounced with higher axial velocities and a more narrow deficit. The profile at $z/D = 1.50$ now also shows a wake-like profile with a wide deficit. At $t/t_{cyc} = 0.25$ all profiles except the $z/D = 4.00$ profile have attained wake-like shapes. The profiles close to the ports are characterized by a more narrow deficit and higher maximum velocities. The axial profile at $z/D = 4.00$ is approximately constant. At $t/t_{cyc} = 0.30$ the axial deficit at the two first axial positions have increased resulting in negative axial velocities near the cylinder axis. This shows that a central swirl induced recirculation zone has been created, which is also known as a vortex breakdown. For $t/t_{cyc} = 0.32$–0.34, the deficit becomes more narrow and the central recirculation disappears. The last axial profile has now also attained a wake-like shape. At $t/t_{cyc} = 0.40$ the ports are closed and a significant change in the axial velocity profiles are observed. The profiles still have a wake-like shape but the maximum velocities are significantly reduced, the deficit has become significantly wider, and negative centerline velocities are observed for all axial positions. For the remaining times during the standstill period $t/t_{cyc} = 0.50$–1.00, the centerline velocity is observed to change between positive and negative values. This phenomenon seem to be complex and sometime results in positive centerline velocities at one axial position

Figure 7: Radial profiles of phase-averaged velocity for different times during the cycle. (*top row*) Tangential velocity V_θ/V_b, (*bottom row*) axial velocity V_z/V_b. The figure is continued on Figure 8.

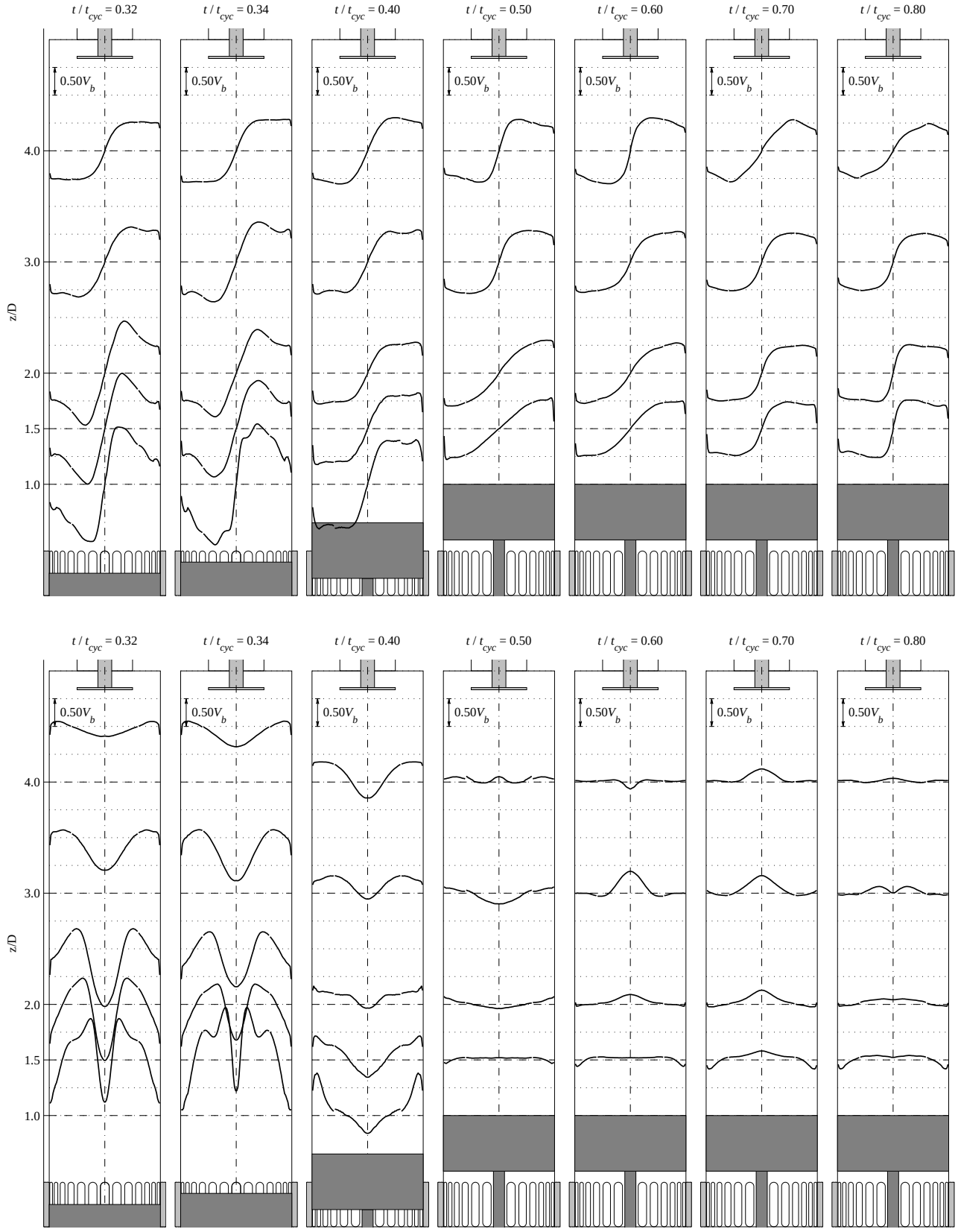

Figure 8: See facing page for caption

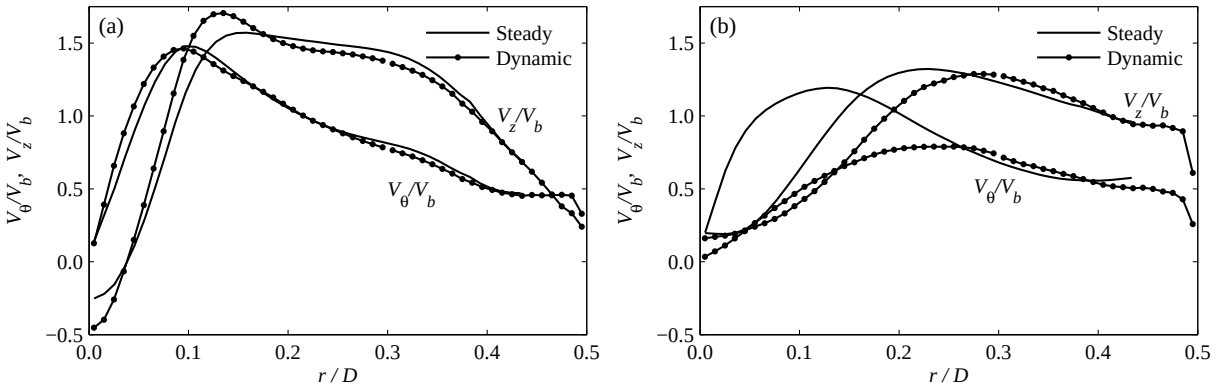

Figure 9: Comparison of radial velocity profiles for the steady-flow case [7] and the dynamic case at $t/t_{cyc} = 0.30$ for axial positions of (a) $z/D = 1.00$ and (b) $z/D = 2.00$.

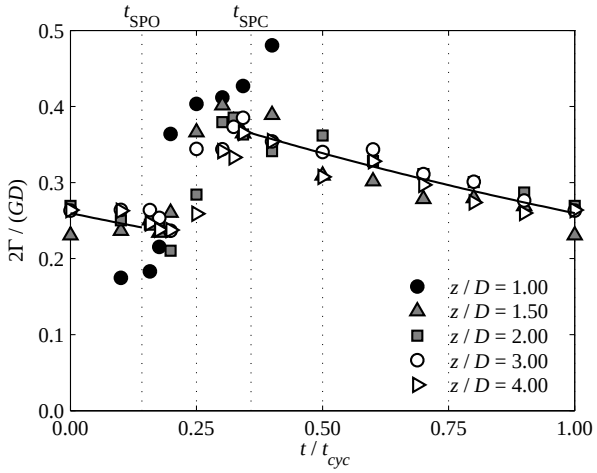

Figure 10: Normalized angular momentum as a function of time for different axial positions. The *solid line* shows fit with exponential decay

and negative centerline velocities at the next position e.g. for $t/t_{cyc} = 0.60$ at $z/D = 3.00$ and $z/D = 4.00$. Animations of time resolved LDA profiles indicate that the changing centerline velocities are the result of large swirl induced coherent structures moving around in the cylinder.

3.4 Comparison of dynamic and steady-flow case

In the previous section it was shown that at $t/t_{cyc} = 0.30$ the tangential velocity profiles in the bottom of the cylinder have a shape similar to the profiles under steady-flow conditions. To investigate to which degree the flow under steady-flow conditions represents the flow under dynamic conditions a comparison is carried out between the steady-flow profiles and the dynamic profiles. In Figure 9 the comparison is shown for the axial positions $z/D = 1.00$ and $z/D = 2.00$ using the dynamic profiles from $t/t_{cyc} = 0.30$. For $z/D = 1.00$ it is observed that there is a good agreement between the steady-flow and dynamic profiles, with the best agreement seen for the tangential velocity profiles. However, the differences between the profiles increase as a function of axial position which can be seen from Figure 9b. The tangential velocity for the steady-flow case shows a higher gradient near the center and has a maximum velocity approximately 1.5 times higher than the dynamic profile. It can thus be concluded that the profiles measured under steady-flow conditions in general will not be representative for the flow under dynamic conditions.

3.5 Angular momentum

The generation and decay of swirl in the cylinder is investigated by calculating the angular momentum from the radial profiles of tangential velocity at the different axial positions. The angular momentum per unit length is given by

$$\Gamma(z,t) = \int_{A_{cyl}} \rho V_\theta r \, dA = 2\pi \int_0^{D/2} \rho V_\theta(r) r \, r \, dr \tag{1}$$

The angular momentum for the five axial positions are presented as a function of time in Figure 10. In the figure the angular momentum is normalized using the cylinder radius and the axial momentum at $t/t_{cyc} = 0.25$ which is given by $G = \rho A_{cyl} V_b$. After scavenge port opening a general increase in angular momentum is observed. The axial positions closest to the scavenge ports show the increase first and also show the highest levels of angular momentum. From scavenge port closing until scavenge port opening the angular

momentum shows a monotonic decreasing trend and a reduction in the the axial variation. Turbulent swirling flows in pipes are known to show an exponential decay [10, 11]. The decay rate of the swirl is estimated by fitting an exponential function of the form $\Gamma(t) = \Gamma_0 \exp(-\lambda t/t_{cyc})$, where λ is the decay rate, to the angular momentum from port closing to port opening. The decay rate is found to be $\lambda = 0.53$ corresponding to a reduction of 34% from scavenge port closing to scavenge port opening. For engines it is reported that typically 25–33% of the initial swirl is lost at TDC [5] which agrees well with the model result.

4. Conclusions

The turbulent swirling flow in a dynamic scale model of a large two-stroke low-speed uniflow-scavenged marine Diesel engine is investigated experimentally. The flow is characterized using phase-locked stereoscopic particle image velocimetry (PIV) and laser Doppler anemometry (LDA). Radial velocity profiles are generated from the PIV data and the accuracy of the profiles are evaluated through repeated measurements and comparison with LDA. The main conclusions of the work are as listed below

- A database of experimental results suitable for CFD validation purposes is established. The experimental velocity profiles are shown to have an uncertainty corresponding to approximately 3% of the bulk velocity at fully open ports.
- The temporal development of the in-cylinder flow is shown to be highly complex. In the period where the ports are closed, the tangential velocity profiles are characterized by a central region with approximately solid body rotation and an annular region with approximately constant velocity. In the same period, the axial velocity profiles show non-zero velocities indicating that large unsteady swirl induced flow structures exist.
- Comparison of profiles obtained under steady-flow and dynamic conditions, shows that results obtained under steady-flow conditions in general will not be representative for the flow in the dynamic model.
- The swirl strength is investigated by computing the angular momentum from the tangential velocity profiles. The swirl strength shows an exponential decay from scavenge port closing to scavenge port opening corresponding to a reduction of 34%.

REFERENCES

[1] Gordon P. Blair. *Design and Simulation of Two-Stroke Engines*. SAE International, 400 Commonwealth Drive, Warrendale, 1996.

[2] R. Diwakar. Three-dimensional modeling of the in-cylinder gas exchange processes in a uniflow-scavenged two-stroke engine. *SAE Tech. Paper Ser.*, page 870596, 1987.

[3] S. Scott Goldsborough and Peter Van Blarigan. Optimizing the scavenging system for a two-stroke cycle, free piston engine for high efficiency and low emissions: A computational approach. *SAE Tech. Paper Ser.*, 1:1–22, 2003.

[4] S. Haider, T. Schnipper, A. Obeidat, K. E. Meyer, V. L. Okulov, S. Mayer, and J. H. Walther. PIV study of the effect of piston position on the in-cylinder swirling flow during the scavenging process in large two-stroke marine Diesel engines. *J. Mar. Sci. Tech.*, 18:133–143, 2013.

[5] J. B. Heywood. *Internal combustion engine fundamentals*. McGraw Hill, Inc., 1988.

[6] J. Hult and S. Mayer. A methodology for laser diagnostics in large-bore marine two-stroke diesel engines. *Meas. Sci. Technol.*, 24(4):1–10, 2013.

[7] K. M. Ingvorsen, K. E. Meyer, J. H. Walther, and S. Mayer. Turbulent swirling flow in a model of a uniflow scavenged two-stroke engine. *Exp. Fluids*, 54:1494, 2013.

[8] Kristian M. Ingvorsen, Knud Erik Meyer, Teis Schnipper, Jens H. Walther, and Stefan Mayer. Swirling flow in model of large two-stroke diesel engine. In *16th Int. Symp. on Applications of Laser Techniques to Fluid Mechanics*, Lisbon, Portugal, July 2012.

[9] S. Jakirlić, K. Hanjalić, and C. Tropea. Modeling rotating and swirling turbulent flows: A perpetual challenge. *AIAA J.*, 40(10):1984–1996, 2002.

[10] Osami Kitoh. Experimental study of turbulent swirling flow in a straight pipe. *J. Fluid Mech.*, 225:445–479, 1991.

[11] Frank Kreith and O. K. Sonju. The decay of a turbulent swirl in a pipe. *J. Fluid Mech.*, 22(2):257–271, 1965.

[12] Hiroshi Nakagawa, Satoshi Kato, Mataji Tateishi, Takeshi Adachi, Harutaka Tsujimura, and Masayoshi Nakashima. Airflow in the cylinder of a 2-stoke cycle uniform scavenging diesel engine during compression stroke. *Jpn. Soc. Mech. Eng.*, 33(3):591–598, 1990.

[13] A. Obeidat, S. Haider, K. E. Meyer, and J. H. Walther. Large eddy simulations of the influence on piston position on the swirling flow in a model Diesel engine. *Int. J. Num. Meth. for Heat & Fluid Flow*, 2013. accepted.

[14] W. H. Percival. Method of scavenging analysis for 2-stroke-cycle diesel cylinders. *SAE Trans.*, 63:737–751, 1955.

[15] P. H. Schweitzer. *Scavenging of two-stroke cycle Diesel engines*. Macmillan Publishing Company, 1949.

[16] E. Sher, I. Hossain, Q. Zhang, and D. E. Winterbone. Calculation and measurements in the cylinder of a two-stroke uniflow-scavenged engine under steady flow conditions. *Exp. Therm. Fluid Sci.*, 4:418–431, 1991.

[17] E. Sigurdsson, K. M. Ingvorsen, M. V. Jensen, S. Mayer, S. Matlok, and J. H. Walther. Numerical analysis of scavenge flow and convective heat transfer in large two-stroke marine diesel engines. *Appl. Energy*, 2013. in preparation.

[18] W. Steenbergen and J. Voskamp. The rate of decay of swirl in turbulent pipe flow. *Flow Mea. Instru.*, 9(2):67–78, 1998.

[19] Nak Won Sung and Donald J. Patterson. Air motion in a two stroke engine cylinder — the effects of exhaust geometry. *SAE Trans.*, pages 2534–2544, 1982. Paper No. 820751.

[20] T. Uzkan. The effects of engine speed on the scavenging characteristics of a two-cycle engine. *J. Engng. Gas Turbines and Power*, 110:523–530, 1988.

[21] Hugh D. Young and Roger A. Freedman. *Sears and Zemansky's university physics: with modern physics*. Addison-Wesley Publishing Company, Sansome St., San Fransico, 11 edition, 2004.